https://doi.org/10.1016/j.seppur.2017.04.016
This is the Pre-Published Version.

# Titanium-Zinc-Bismuth Oxides-Graphene Composite Nanofibers as High-Performance Photocatalyst for Gas Purification

Carina Chun Pei, Kenneth Kin Shing Lo, Wallace Woon-Fong Leung*

Department of Mechanical Engineering, The Hong Kong Polytechnic University, Hung Hom, Hong Kong

*Correspondence to: mmleung@polyu.edu.hk

**Abstract:** Novel technologies have been on demand to develop improved photocatalyst for gas purification. Graphene has been used to improve the performance of photonic devices based on its high charge conductivity as well as other unique properties. Traditional approach uses discrete graphene sheets with sparse, sporadic deposition of semiconductor crystals ($TiO_2$) as photocatalyst, which results in poor light harvesting and electron-hole recombination at the sheet edges. In our novel configuration, the edge effect has been eliminated by having the graphene sheets being rolled into a "spiral" inserted in the 80nm $TiO_2$/ZnO/$Bi_2O_3$ (TZB) nanofiber, and free electrons can only travel unidirectional along the axis of the nanofiber. The nanofiber is fabricated with its surface packed with 10-nm sized TZB nanocrystallites that increases the surface area thereby improving light harvesting. Further, the addition of ZnO and $Bi_2O_3$ reduce the band-gap energy of the composite facilitating harvesting of the visible light spectrum. Other than fast transport of electrons to sites where photocatalysis is needed, the graphene roll (exposed in between the pores of the TZB nanocrystallites) is proven to

© 2017. This manuscript version is made available under the CC-BY-NC-ND 4.0 license http://creativecommons.org/licenses/by-nc-nd/4.0/

harvest more energy from the entire UV-vis spectrum and almost double the already large surface area of the nanofibers. Note the larger surface area of the photocatalyst facilitates pollutant gas molecule adsorption, which is the first and an important step prior to photocatalysis. The TZB-Gr photocatalyst, after optimized with as much as 26.5% by mass of graphene in the nanofibers, has superior photoactivity in degradation of NO under solar irradiation. It is 35% higher than nanofibers with just TZB alone, and at least 17% higher than traditional approach with discrete graphene sheets (with edge effect) with TZB particles deposited on the sheet, and 10 times better than 25-nanometer $TiO_2$ nanoparticles. Other photonic and non-photonic devices, such as bio-chemical sensors, can also benefit from the innovative configuration of semiconductor nanofibers with inserted graphene for the low band-gap energy, fast charge transit, long electron life time, reduced recombination rate, and large surface area.

**Keywords:** $TiO_2$/ZnO/$Bi_2O_3$-graphene nanofibers; solar-light driven photocatalyst, charge transport and recombination, titanium dioxide, nitric oxide

## Introduction

Efficient photocatalytic processes have attracted tremendous increase in interest. In particular, titanium dioxide ($TiO_2$) with strong oxidizing power, biological and chemical inertness, and low cost, has proven to-date to be the most suitable photocatalyst. Despite this, the rapid recombination rate of photogenerated electron−hole pairs in $TiO_2$ results in low quantum efficiency, thereby limiting its practical application. During the past decade, a variety of remedial strategies have been

developed to improve the photocatalytic performance of semiconductor photocatalysts, for example, improved textural design[1, 2], doping[3, 4], noble metal loading[5, 6] and novel semiconductor composites[7, 8]. Further, numerous attempts have been made to incorporate carbonaceous nanomaterials with semiconductor photocatalysts to enhance their photocatalytic performance, which potentially offers improved electron-hole separation efficiency. Recently, as a result of the high specific surface area and superior electron mobility of graphene, extensive efforts have been devoted to combine graphene with semiconductor photocatalysts to enhance their catalytic performance. The pioneer work of Kamat and co-workers in synthesizing $TiO_2$ nanoparticles deposited on graphene sheets[9] (shown in scheme 1a) has stimulated incessant research activities[4] in the preparation, modification, and application of graphene-based photocatalytic composites. Because of the unique properties of graphene, the composite incorporating graphene simultaneously covered three excellent unique advantages: increased pollutants adsorption, extended light absorption range, and facile charge transport and separation. Subsequently, researchers exclusively adopted such configuration for photocatalytic application[10-13]. However, this configuration is problematic as the edges of the 2D graphene sheet act as recombination sites. More damaging, the discrete individual graphene sheet renders a discontinuity for electron transport. Also, the non-uniform sporadically distribution of $TiO_2$ nanoparticles on these graphene sheets further limits light harvesting.

These aforementioned drawbacks are overcome in our novel architecture by inserting graphene sheet in a compact, spiral roll in the core of the $TiO_2$/ZnO/$Bi_2O_3$ composite

nanofibers (abbreviated hereafter as TZB nanofibers which acts as a shell) to increase electron−hole pair separation and charge transport as illustrated in Scheme 1b. Not only improving light harvesting due to the combination of $TiO_2$, ZnO, $Bi_2O_3$ and graphene, this configuration also eliminates the edge effect and more importantly provides for the electrical charges a well-defined transport path along the TZB nanofiber axis.

**Methodology**

Materials

Titanium tetra-isopropoxide (TIIP), zinc acetate dehydrate, bismuth(III) nitrate pentahydrate, polyvinyl pyrrolidone (PVP) (MW= 1,300,000), graphite powder (<20ìm), isometric acetic acid and benchmark test $TiO_2$ nanoparticles (Degussa P25) were all purchased from Sigma–Aldrich, while ethanol was purchased from Advanced Technology & Industrial Company. All reagents were of analytical grade and used without any further purification.

Fabrication

5% PVP was dissolved in ethanol assisted by ultrasonic stirring. 10 wt. % graphite was added to the solution and blended with a Philips HR2096 blender at 21,000 rpm. The turbulence induced shearing caused the graphitic planes to slip relative to each other until full exfoliation was achieved, resulting in free floating graphene. The graphene was subsequently bound to the PVP in the solution, preventing re-aggregation of graphene into graphite. The solution was typically blended for 20 min until a suspension

of graphene and graphite was formed. The suspension was subsequently centrifuged at 9,993 G (1 G = 9.81m/$s^2$) for 2 to 15 min to removal denser residual to obtain pure graphene suspension[14] in the supernatent. The amount of graphene for insertion in the nanofibers by subsequent electrospinning was controlled by the time duration of the centrifugation, with more graphene in shorter duration and less graphene in longer duration of centrifugation.

3 vol. % $Ti(OiPr)_4$ and isometric acetic acid, together with $Zn(CH_3COO)_2{\cdot}2H_2O$ and $Bi(NO_3)_3{\cdot}5H_2O$, were then added to the suspension to form the precursor solution for electrospinning.

Electrospinning using nozzle-less setup was carried out under the following conditions: supplied voltage, 70 kV; electrode-to-collector distance, 19 cm; and electrode rotating speed, 30 Hz. The resulting electrospun fibers were treated for 2 h at 600ºC to obtain the TZB-Gr composite nanofibers.

Photocatalytic measurement

The photocatalytic activity experiments for the removal of NO in air were performed in a continuous flow reactor at ambient temperature. The reactor tank has a height of 10 cm, length 30 cm and width 15 cm (total volume 4.5L) and was made of stainless steel and covered with Saint Glass. Samples dish (150 × 25 mm) containing the catalyst nanofibers were placed in the center of the reactor. A 300W commercial tungsten halogen lamp (General Electric) was used as the simulated solar light source, which

was vertically positioned above the sample dish outside the reactor. The integrated ultraviolet (UV) intensity in the range 310 to 400nm was 720±10 $\mu Wcm^{-2}$. Four mini-fans were mounted around the lamp to stabilize the temperature of the test flow system during the photocatalytic oxidation reaction. The NO gas was introduced to the flow reactor from a compressed gas cylinder at a concentration of 50.1 ppm NO (BOC Gas) with nitrogen balance. To simulate a real-world polluted environment, the initial concentration of NO was diluted to about 250 ppb by the air stream supplied by a zero air generator (Thermo Environmental Inc. Model 111). The relatively humidity level of the NO stream was controlled by flowing the zero air streams through a humidification chamber. The gas streams were premixed completely by a gas mixer, and the flow rate was controlled at 3 L $min^{-1}$ by a mass flow controller. The residence time was adjusted accordingly by changing the flow rate. The lamp was turned on after the adsorption–desorption equilibrium was reached among water vapor, gases, and photocatalysts. The concentration of NO was continuously measured by a chemiluminescence NO analyzer (Thermo Environmental Instruments Inc. Model 42c), which can monitor NO, $NO_2$, and NOx with a sampling rate of 0.7 L $min^{-1}$. The removal rate (%) of NO was calculated from the concentration of NO, respectively, in the feed and outlet streams. The reaction of NO with air in the absence of photocatalyst was negligible in a control experiment, with or without light.

Characterization

The morphologies of nanofibers were investigated using scanning electron microscope

(SEM) (JEOL Model JSM-6490) and transmission electron microscopy (TEM) (JEOL Model JEM-2011).

Specific surface areas were examined by Brunauere–Emmette–Teller (BET) test using $N_2$ adsorption at 77K using Beckman Coulter SATM 3100.

X-ray photoelectron spectroscopy (XPS) was conducted using a Physical Electronics 5600 multi-technique system.

Raman spectrum was performed by Horiba HR 800.

UV–vis diffuse reflectance spectra (DRS) were measured and recorded by a Varian Cary 100 Scan UV–Vis system equipped with a Lab sphere diffuse reflectance accessory to obtain the reflectance spectra of the catalysts over a range of 200 to 800 nm. $BaSO_4$ (Lab sphere USRS-99-010) was used as a reference in the measurement. The measured spectra were converted from reflection to absorbance by the Kubelka–Munk equation.

Photoluminescence (PL) spectra were recorded using an Edinburgh FLSP920 spectrophotometer.

Electrochemical impedance spectroscopy (EIS) measurement was carried out with electrochemical workstation (CH Instruments CHI660c). The TZB film was peeled off from the glass slide after 2 h heat treatment and subsequently transferred to another FTO glass precoated with an ultra-thin adhesive layer of $TiO_2$ paste. The device for the

EIS testing was obtained after it was calcinated again at 450 ºC for 2 h. The thickness was determined to be 20μm from Surface Profilometer (VeekoDektak 8) and the active area was 0.15 $cm^2$.

Intensity-modulated photovoltage spectroscopy (IMVS) and intensity-modulated photocurrent spectroscopy (IMPS) were executed using a Zahner CIMPS photo-electrochemical workstation (Zahner-Elektrik) controlled by CIMPS and Thales Z software packages(Zahner-Elektrik). The photo-anodes were backlit with a 370 nm LED, 20 $Wm^{-2}$. In the IMVS experiments, the ac frequency scanned from 500 Hz → 1 kHz → 100 mHz. In IMPS experiments, the AC frequency range is run from 100 Hz → 10 kHz →1 Hz. In both measurements, 10 measuring steps (frequencies)/decade were carried out in the tests. Five measurement points were averaged at <66 Hz with 20 points averaged per measurement frequency at higher frequencies.

The thermal decomposition behavior of TZB and TZB-Gr were examined using a thermo gravimetric analyzer and differential scanning calorimeter (TGA–DSC) (Netzch) under ambient pressure in the temperature range between 30ºC and 900ºC at a controlled heating rate of 10ºC $min^{-1}$.

**Results and Discussion**

Fig. 1 compares the NO removal rate as function of irradiation time for, respectively, TZB-Gr nanofibers with different contents of incorporated graphene, TZB nanofibers, and P25 $TiO_2$ nanoparticles. The tests were carried out under simulated solar-light

irradiation with single-pass, flow-through reactor. After 30 min simulated solar-light irradiation, 76.4%, 89.2%, 86.6%, 84.0%, 73.1% and 68.5% of NO gas was oxidized by the TZB-Gr nanofibers prepared with 2 min, 3 min, 4 min, 5min, 10 min, and 15 min centrifugation, respectively. The performance for all the nanofiber photocatalysts with graphene were higher than 67.2% conversion recorded with just the TZB nanofibers without graphene. There are two important findings. First, insertion of graphene helps photocatalysis. Second, there is an optimal amount of graphene in the nanofibers that yields the most optimal performance. The basis for these enhancements will be confirmed by the analytical characterization to be discussed subsequently. For reference on performance, the gold standard for P25 $TiO_2$ nanoparticles yielded a disappointing of only 8.5% conversion.

Furthermore as shown in Fig. 1, the NO removal rate for TZB nanofibers increased rapidly in the first 5 min and reached ultimately the highest value and thereafter maintained constant thereafter for at least 30 min. On the other hand, it took 15 min for $TiO_2$ nanoparticles to achieve the highest NO conversion of 8.5%, and subsequently the conversion rate decreased slowly to 6% at 30 min. The latter was ascribed to the accumulation of nitric acid ($HNO_3$) on the particles surface resulting in deactivation of photo-catalyst. In general, the TZB-Gr composite nanofibers with 3-min centrifugation (highest graphene in nanofibers) reached the highest photocatalytic efficiency, which is 35% improvement above-and-beyond that of pure TZB nanofibers and having a whopping increase of 10 times above that of the benchmark P25 nanoparticles (pure $TiO_2$ of 25nm diameter) on the conversion of NO. It is noteworthy to point out that

analytical characterization and photocatalysis application both reveal consistently that TZB-G composite with the highest graphene in the nanofibers (3-min centrifugation sample) has both the best characteristics and the best photocatalytic performance. The results of the analytical characterization will be discussed next.

Fig. 2 shows images of the TZB-Gr nanofibers acquired using SEM and TEM. Fig. 2a-2f are the SEM images corresponding to the TZB-Gr nanofibers with different graphene in precursor suspension centrifuged at various time durations, 2 min, 3 min, 4 min, 5 min, 10 min, and 15 min, respectively. As seen in all these figures, the electrospun nanofibers with diameter of 80 nm are randomly distributed in layers, which are confirmed by the low magnification TEM images. Graphene flakes can be seen in Fig. 2a, which reveals excess graphene in the TZB nanofibers in the 2-min centrifuged sample. Note graphene is not visible from all the other SEM images which suggests that graphene, in lesser amount than the 2-min sample, are all incorporated in the TZB nanofibers. It can be argued that our 2-min sample is somewhat analogous to the Kamat's configuration for which $TiO_2$ nanoparticles (in our case TZB nanoparticles) are sporadically deposited on the "spread-out" 2D graphene sheets. The photocatalytic performance for the Kamat configuration (see Schematic 1a and Fig. 2a) is not as high. It is at least 15% conversion efficiency below (2-min centrifugation from Fig. 1) when compared to our present configuration (see Schematic 1b) with 3-min centrifugation shown in Fig. 1. Unlike the open graphene sheet with edge effects, in the present

configuration the graphene sheets are rolled up inside the TZB nanofibers eliminating the edge effects and also the nanofiber surface is closely packed with TZB nanocrystals fully interfacing with the rolled-up graphene inner roll. From the TEM images in Fig. 2h, the electrospun TZB nanofibers that have incorporated graphene exhibit clear crystal lattice fringes. Indeed, the crystal inter-planar spacing of $TiO_2$ grains is determined to be about 0.35 nm, which corresponds to the (101) planes of the anatase phase[15]. On the other hand, the crystal inter-planar spacing of 0.341 nm corresponds to graphene[16, 17]. The graphene sheets were spirally rolled up during electrospinning inside the TZB nanofibers. The forgoing morphology analysis indeed confirmed that graphene sheets were inside the TZB nanofibers.

The specific surface areas of TZB nanofibers with and without graphene have been determined by the BET test with results listed in Table 1. Despite the TZB nanocrystallites are packed compactly around the rolled-up graphene sheets forming a shell; there are numerous exposed nano-sized openings in between these nanocrystallites. Through these openings, the surface area of the composite nanofibers can be increased greatly since graphene has a tremendous large specific surface area. As can be seen from the measurements, the surface area of TZB-Gr nanofibers almost doubles that of TZB nanofibers without graphene. The photocatalytic activity can be certainly enhanced by adsorption of pollutant gas molecules (NO molecules in our test) onto the catalyst surface, which is an essential step in photocatalysis.

The XPS spectra (See Fig. 3) of TZB nanofibers with and without graphene were

measured to further confirm the presence of graphene. The results reveal that the C 1s peak of the nanofibers with graphene was stronger than that without, which confirms that graphene was successfully incorporated in the TZB nanofibers. Moreover, the binding energy of 284.8 eV was a typical peak position for graphene carbon[18, 19], which demonstrated the $sp^2$ hybridized carbon in the graphene state. Furthermore, the deconvoluted peaks centered at the binding energy of 285.9 and 289.0 eV, respectively, which were attributed to the C–O and C=O oxygen containing carbonaceous bonds. The TZB-Gr nanofibers show three distinct peaks at 284.8, 285.7, and 289.3 eV, which corresponds to C–C in graphene, C–O, and C=O bonds, respectively. On the other hand, only the C–O and C=O bonds were detected in the TZB nanofibers. Furthermore, lower amounts of the oxygen-containing carbonaceous bands were detected in the carbon peak of TZB because the peak area of C−O and C=O bonds was obviously decreased, indicating fewer oxygen deficiencies. It is evident that when compared with TZB nanofibers, TZB-Gr nanofibers exhibit more oxygen deficiencies on the surface indicating more reacting sites[20], thus higher photocatalytic activity.

Raman spectroscopy is one of the most important tools used for the characterization of carbon-based materials. The Raman spectra of TZB and TZB-Gr composite nanofibers are shown in Fig. 4a. It can be seen that there are two peaks around 1350 and 1580 $cm^{-1}$ [13, 20, 21] in TZB-Gr spectrum, corresponding respectively to the D peak associated with edge defects and the G peak associated with highly ordered graphite. The G peak has split into $G^-$ and $G^+$ peaks (as can be seen that the peak is not quite symmetrical about its center line), reflecting the strain of graphene sheets being rolled up inside the

TZB nanofiber core. The 2D peak is at approximately 2700 $cm^{-1}$, with intensity and shape related to the morphology and thickness of the graphene sheet. The approximate symmetrical Gaussian distribution suggested the existence of bilayer graphene[9, 22, 23]. Given the above, the Raman spectrum further confirmed the configuration of the TZB-Gr composite nanofibers with bilayer graphene sheets spirally inserted inside the TZB nanofiber shells.

The DRS of TZB-Gr nanofibers, TZB nanofibers and P25 $TiO_2$ nanoparticles are all compared in Fig. 4b. From the absorption spectra between 200 and 700 nm, the absorbance of TZB-Gr nanofibers in the UV range have been significantly improved, and the absorption edges have been shifted to the visible region[24-26] . Using the Kubelka–Munk equation, the band gap of TZB-Gr nanofibers, TZB nanofibers, $TiO_2$ nanoparticles were determined to be 2.30 eV, 2.72 eV and 3.20 eV, respectively. As a result of the extended photo-responding range, more efficient utilization of the solar spectrum can be achieved with TZB-Gr nanofibers. The solar photocatalytic activity of TZB-Gr is expected to facilitate its use in practical environmental remediation.

The PL spectra of semiconductors are useful to shed light on the migration, transfer, and recombination processes of the photogenerated electron–hole pairs[26, 27]. The PL emission is mainly attributed to the recombination of the excited electrons and holes. PL signals for TZB-Gr composite nanofibers with different centrifuged time durations of the precursor suspension and TZB composite nanofibers are given in Fig. 4c. Compared with TZB nanofibers, the TZB-Gr composite nanofibers exhibit lower PL

intensities, indicating that the recombination of the photoinduced charge carriers was inhibited effectively from the introduction of graphene in the TZB nanofibers. Interestingly, the lowest PL intensity for TZB-Gr composite nanofibers with 3-min centrifugation (most graphene content in the nanofibers among all samples) indicates the lowest recombination rate of photoinduced electron−hole pairs[28]. This may be related in-part to the efficient transport of electrons along the graphene based TZB nanofibers.

Fig. 5a shows the EIS Nyquist plots of the as-prepared TZB-Gr composite nanofibers with different centrifuged time durations and TZB composite nanofibers. The radius of the "semi-circle" on the EIS Nyquist plot of TZB-Gr with 3-min centrifugation, with the highest graphene in the nanofibers, is the smallest among all the samples. In the EIS Nyquist plot, the smaller semi-circle size indicates an effective separation of photogenerated electron−hole pairs and fast interfacial charge transfer to the electron donor or acceptor. Since the radius of the arc on the EIS spectra reflects the reaction rate occurring at the surface, it suggests that a more effective separation of photogenerated electron−hole pairs and the fastest interfacial charge transfer occurring for the TZB-Gr composite nanofibers with the highest graphene content (i.e. 3-minute centrifugation) under this condition[30]. This result clearly indicates that the synergistic combination of TZB and graphene can effectively retard recombination by enhancing the separation of photogenerated electron−hole pairs[11, 29].

The IMVS data for TZB-Gr nanofibers with different centrifuged durations and TZB

nanofibers reveal that the TZB nanofibers ($\tau_n$ = 0.17s at 20 W $cm^{-2}$) have the shortest lifetime. On the other hand, TZB-Gr nanofibers especially with 3-min centrifugation with the highest graphene ($\tau_n$ = 0.51 s at 20 Wcm-2) has approximately 3-fold longer lifetime, see Fig. 5b. This also reveals the possibility that graphene may have storage capacitance for electrons resulting in such 3-fold increase in electron lifetime.

The electron diffusion constant $\tau_D$ can be determined from IMPS, see Fig. 5c. The electron transit time of TZB nanofibers is about 13.31 ms, while TZB-Gr with 3-min centrifugation (highest graphene) is much shorter, only 3.14 ms. The trend clearly shows longer lifetime and shorter transit time for electrons with increasing presence of graphene in the precursor solution (or more specifically more graphene in the nanofibers as the 2-min sample had the most graphene in suspension but during calcination, due to the differential expansion, this results in explosion of nanofibers converting to Kamat's configuration of graphene sheet/flakes with sporadic semiconductor nanoparticles on the graphene/flakes). It is evident that increasing IMVS electron lifetimes and decreasing IMPS electron transit times represent possible electron storage capacitance of graphene, more effective electron transport, and reduced electron trapping for charge recombination[30-32]. TZB-Gr with 3-minute centrifugation and highest graphene content in the nanofibers holds the longest lifetime and shortest transit time, revealing the most efficient electron transport and the least charge recombination, thus results in the best photocatalytic efficiency.

Finally, it is interesting to determine the amount of graphene in the nanofibers given the

impressive performance that have been realized. To answer this issue, the TGA-DSC measurements for the TZB and TZB-Gr, respectively, revealed some rather remarkable results on the amount of graphene inside the TZB-Gr nanofibers. This is shown in Fig. 6 and some important observations can be made from the figure.

1. The DSC curve for both TZB and TZB-Gr reveal two exothermic peaks, first exothermic peak occurs between 300-400$^{o}$C, corresponding to decomposition of PVP and some smaller organic molecules. The second exothermic peak occurs between 450 and 550$^{o}$C, with the one for the TZB-Gr being deferred even slightly at a higher temperature. This second peak corresponds to complete decomposition of PVP and any smaller organic molecules for both samples. However, between 550 to 750$^{o}$C, there is a moderate broad exothermic peak only for the TZB-Gr but not with TZB. This indeed corresponds to combustion of the graphene in the TZB-Gr nanofibers. This range also matches with that of the literature of burning carbonaceous materials.
2. The TGA curve for the TZB shows a rather substantial decrease in mass up to 100$^{o}$C from start at 30$^{o}$C due to evaporation of water in the nanofibers. On the other hand, this is rather insignificant for the TZB-Gr. A plausible reason is that liquid may be trapped in the hollow TZB core whereas the TZB-Gr is already filled with graphene in their core allowing no extra room for trapped water.

3. Corresponding to the two exothermic peaks, there is a significant decrease in mass in both the TZB and TZB-Gr nanofibers due to decomposition of PVP.
4. After reaching 500$^{o}$C, there is no further loss in mass for the TZB, yet between 550 and 750$^{o}$C, the graphene in the TZB-Gr nanofibers start to burn until completion of combustion at 750$^{o}$C. The mass decreases continuously during this combustion process.
5. From the beginning (at 550$^{o}$C) to the end (at 750$^{o}$C), the total mass loss from combustion of graphene is 0.7432g with a remaining residual (non-burnable TZB) of 2.0602g. Beyond 800$^{o}$C, the combustion of any organic matters has been completed and there is no further mass loss in TZB-Gr nanofibers. Therefore, the graphene by mass in the nanofibers is simply 26.5% (= 0.7432 / [0.7432+2.0602]). This case corresponds to the 3-min centrifugation, i.e. the maximum graphene amount that can be inserted into the 80-nm diameter nanofibers without exploding during calcination. (Other centrifugation times would only have lesser graphene contents.) This also corresponds to the best performer among all nanofibers with different centrifugation times/graphene contents. This high percentage of graphene beyond 20% is rather unexpected!
6. Interestingly as shown in Fig. 6, the TZB-Gr nanofibers that were prepared were calcinated at 600$^{o}$C for which the combustion of carbon has just started without significantly burning off the in-situ graphene in the nanofibers. At this temperature, some of the anatase phases have been converted to rutile phases that have larger crystals favoring photocatalysis.

## Conclusions

In summary, TZB-Gr composite nanofibers with TZB nanofiber as a shell and bilayer graphene spiral roll in the nanofiber core have been prepared successfully via a sol-gel based electrospinning process. The composite nanofibers have demonstrated to have excellent photocatalytic performance. SEM and TEM observations indicate that graphene sheets are fully exfoliated and spiraled inserted in the TZB nanofibers, which are confirmed by Raman plot. Not only this unique novel configuration greatly increases the specific surface area, it also reduces band-gap energy, retards electron-hole recombination, and speeds up charge transport. The electron lifetime and electron mobility are enhanced in this unique configuration, which are revealed in IMVS, IMPS and EIS. The photocatalytic activity measurements demonstrate that the optimal TZB-Gr photocatalysts (with as much as 26.5% graphene by mass) have superior photoactivity in degradation of NO under solar irradiation, which is 35% higher than TZB and at least 10 times better than the benchmark $TiO_2$. The significant enhancement in photoactivity can be ascribed to the efficient separation and transport of photogenerated carriers in the TZB-graphene coupled system, and the concerted effects of individual components, or their integrated synergistic properties.

## Acknowledgement

We thank the financial support in part from the Hong Kong Innovation Technology Commission under Project #UIM/280 on the project “Development of Next Generation Multi-layer Chitosan Nanofiber Filters for Medical/Environmental Use with Novel

Filtration/Purification Technology".

**References**

[1] J.H. Pan, Q. Wang, D.W. Bahnemann, Hydrous $TiO_2$ spheres: An excellent platform for the rational design of mesoporous anatase spheres for photoelectrochemical applications, Catalysis Today, 230 (2014) 197-204.

[2] M. Meksi, G. Berhault, C. Guillard, H. Kochkar, Design of $TiO_2$ nanorods and nanotubes doped with lanthanum and comparative kinetic study in the photodegradation of formic acid, Catalysis Communications, 61 (2015) 107-111.

[3] Y.-n. Guo, J.-h. Cheng, Y.-y. Hu, D.-h. Li, The effect of $TiO_2$ doping on the catalytic properties of nano-Pd/$SnO_2$ catalysts during the reduction of nitrate, Applied Catalysis B: Environmental, 125 (2012) 21-27.

[4] Q. Dai, S. Bai, J. Wang, M. Li, X. Wang, G. Lu, The effect of $TiO_2$ doping on catalytic performances of Ru/$CeO_2$ catalysts during catalytic combustion of chlorobenzene, Applied Catalysis B: Environmental, 142–143 (2013) 222-233.

[5] M. Khairy, W. Zakaria, Effect of metal-doping of $TiO_2$ nanoparticles on their photocatalytic activities toward removal of organic dyes, Egyptian Journal of Petroleum, 23 (2014) 419-426.

[6] Q. Zhang, D.Q. Lima, I. Lee, F. Zaera, M. Chi, Y. Yin, A Highly Active Titanium Dioxide Based Visible-Light Photocatalyst with Nonmetal Doping and Plasmonic Metal Decoration, Angewandte Chemie International Edition, 50 (2011) 7088-7092.

[7] H. Song, M. Dai, Y.-T. Guo, Y.-J. Zhang, Preparation of composite $TiO_2$–$Al_2O_3$ supported nickel phosphide hydrotreating catalysts and catalytic activity for

hydrodesulfurization of dibenzothiophene, Fuel Processing Technology, 96 (2012) 228-236.

[8] C. Sun, N. Wang, S. Zhou, X. Hu, S. Zhou, P. Chen, Preparation of self-supporting hierarchical nanostructured anatase/rutile composite $TiO_2$ film, Chemical Communications, (2008) 3293-3295.

[9] G. Williams, B. Seger, P.V. Kamat, $TiO_2$-Graphene Nanocomposites. UV-Assisted Photocatalytic Reduction of Graphene Oxide, ACS Nano, 2 (2008) 1487-1491.

[10] S. Min, G. Lu, Dye-cosensitized graphene/Pt photocatalyst for high efficient visible light hydrogen evolution, International Journal of Hydrogen Energy, 37 (2012) 10564-10574.

[11] Z. Sun, J. Guo, S. Zhu, L. Mao, J. Ma, D. Zhang, A high-performance Bi2WO6-graphene photocatalyst for visible light-induced $H_2$ and $O_2$ generation, Nanoscale, 6 (2014) 2186-2193.

[12] X. Guo, C. Hao, G. Jin, H.-Y. Zhu, X.-Y. Guo, Copper Nanoparticles on Graphene Support: An Efficient Photocatalyst for Coupling of Nitroaromatics in Visible Light, Angewandte Chemie International Edition, 53 (2014) 1973-1977.

[13] H. Zhang, X. Lv, Y. Li, Y. Wang, J. Li, P25-Graphene Composite as a High Performance Photocatalyst, ACS Nano, 4 (2010) 380-386.

[14] K.R. Paton, E. Varrla, C. Backes, R.J. Smith, U. Khan, A. O'Neill, C. Boland, M. Lotya, O.M. Istrate, P. King, T. Higgins, S. Barwich, P. May, P. Puczkarski, I. Ahmed, M. Moebius, H. Pettersson, E. Long, J. Coelho, S.E. O'Brien, E.K. McGuire, B.M. Sanchez, G.S. Duesberg, N. McEvoy, T.J. Pennycook, C. Downing, A. Crossley, V.

Nicolosi, J.N. Coleman, Scalable production of large quantities of defect-free few-layer graphene by shear exfoliation in liquids, Nat Mater, 13 (2014) 624-630.

[15] C.C. Pei, W.W.-F. Leung, Photocatalytic oxidation of nitrogen monoxide and o-xylene by $TiO_2$/ZnO/$Bi_2O_3$ nanofibers: Optimization, kinetic modeling and mechanisms, Applied Catalysis B: Environmental, 174–175 (2015) 515-525.

[16] Q. Huang, S. Tian, D. Zeng, X. Wang, W. Song, Y. Li, W. Xiao, C. Xie, Enhanced Photocatalytic Activity of Chemically Bonded $TiO_2$/Graphene Composites Based on the Effective Interfacial Charge Transfer through the C–Ti Bond, ACS Catalysis, 3 (2013) 1477-1485.

[17] B. Jiang, C. Tian, Q. Pan, Z. Jiang, J.-Q. Wang, W. Yan, H. Fu, Enhanced Photocatalytic Activity and Electron Transfer Mechanisms of Graphene/$TiO_2$ with Exposed {001} Facets, The Journal of Physical Chemistry C, 115 (2011) 23718-23725.

[18] F. Meng, W. Lu, Q. Li, J.-H. Byun, Y. Oh, T.-W. Chou, Graphene-Based Fibers: A Review, Advanced Materials, 27 (2015) 5113-5131.

[19] Y. Fu, X. Sun, X. Wang, $BiVO_4$–graphene catalyst and its high photocatalytic performance under visible light irradiation, Materials Chemistry and Physics, 131 (2011) 325-330.

[20] T. Xu, L. Zhang, H. Cheng, Y. Zhu, Significantly enhanced photocatalytic performance of ZnO via graphene hybridization and the mechanism study, Applied Catalysis B: Environmental, 101 (2011) 382-387.

[21] A.S. Wajid, S. Das, F. Irin, H.S.T. Ahmed, J.L. Shelburne, D. Parviz, R.J. Fullerton, A.F. Jankowski, R.C. Hedden, M.J. Green, Polymer-stabilized graphene dispersions at

high concentrations in organic solvents for composite production, Carbon, 50 (2012) 526-534.

[22] Y. Tan, Y. Song, Q. Zheng, Hydrogen bonding-driven rheological modulation of chemically reduced graphene oxide/poly(vinyl alcohol) suspensions and its application in electrospinning, Nanoscale, 4 (2012) 6997-7005.

[23] G. Jung, H.-I. Kim, Synthesis and photocatalytic performance of PVA/$TiO_2$/graphene-MWCNT nanocomposites for dye removal, Journal of Applied Polymer Science, 131 (2014).

[24] Q. Li, X. Li, S. Wageh, A.A. Al-Ghamdi, J. Yu, CdS/Graphene Nanocomposite Photocatalysts, Advanced Energy Materials, 5 (2015).

[25] Q. Xiang, J. Yu, M. Jaroniec, Graphene-based semiconductor photocatalysts, Chemical Society Reviews, 41 (2012) 782-796.

[26] A. Loiudice, J. Ma, W.S. Drisdell, T.M. Mattox, J.K. Cooper, T. Thao, C. Giannini, J. Yano, L.W. Wang, I.D. Sharp, R. Buonsanti, Bandgap Tunability in Sb-Alloyed $BiVO_4$ Quaternary Oxides as Visible Light Absorbers for Solar Fuel Applications, Advanced materials (Deerfield Beach, Fla.), 27 (2015) 6733-6740.

[27] X. Pan, Y. Zhao, S. Liu, C.L. Korzeniewski, S. Wang, Z. Fan, Comparing Graphene-TiO2 Nanowire and Graphene-$TiO_2$ Nanoparticle Composite Photocatalysts, ACS Applied Materials & Interfaces, 4 (2012) 3944-3950.

[28] Q. Xiang, B. Cheng, J. Yu, Graphene-Based Photocatalysts for Solar-Fuel Generation, Angewandte Chemie International Edition, 54 (2015) 11350-11366.

[29] N.O. Weiss, H. Zhou, L. Liao, Y. Liu, S. Jiang, Y. Huang, X. Duan, Graphene: An

Emerging Electronic Material, Advanced Materials, 24 (2012) 5782-5825.

[30] P.A. DeSario, J.J. Pietron, D.H. Taffa, R. Compton, S. Schünemann, R. Marschall, T.H. Brintlinger, R.M. Stroud, M. Wark, J.C. Owrutsky, D.R. Rolison, Correlating Changes in Electron Lifetime and Mobility on Photocatalytic Activity at Network-Modified $TiO_2$ Aerogels, The Journal of Physical Chemistry C, 119 (2015) 17529-17538.

[31] S. Agarwal, A. Greiner, On the way to clean and safe electrospinning—green electrospinning: emulsion and suspension electrospinning, Polymers for Advanced Technologies, 22 (2011) 372-378.

[32] R. Kern, R. Sastrawan, J. Ferber, R. Stangl, J. Luther, Modeling and interpretation of electrical impedance spectra of dye solar cells operated under open-circuit conditions, Electrochimica Acta, 47 (2002) 4213-4225.

**List of Figures**

Scheme 1a Schematic diagram of $TiO_2$ nanoparticles deposited on graphene sheets; 1b Schematic diagram of as-prepared $TiO_2$/ZnO/$Bi_2O_3$-graphene (TZB-Gr) nanofibers.

Fig. 1 The NO removal fraction against irradiation time in the presence of TZB-Gr nanofibers with different graphene centrifuged time durations, TZB nanofibers and P25 nanoparticles.

Fig. 2 SEM and TEM images of TZB-Gr nanofibers after calcination with different graphene centrifuged time durations in precursor solutions: a. 2 min; b. 3 min; c. 4 min;

d. 5 min; e. 10min; f. 15 min. g. TEM image of the prepared nanofibers (3 min); h. HRTEM image of the fibers (3 min).

Fig. 3 The C 1s XPS spectra of TZB-Gr nanofibers and TZB nanofibers.

Fig. 4a Raman spectra of TZB-Gr nanofibers and TZB nanofibers. (Insert shows wavenumber from 1200 to 3000 $cm^{-1}$.) 4b. The UV-Vis absorption spectra of TZB-Gr nanofibers, TZB nanofibers and P25 nanoparticles between 200 and 800 nm. The insert shows the DRS of from the Kubelka–Munk function versus the energy of light. 4c. PL emission spectra TZB-Gr nanofibers with different graphene centrifuged time durations and TZB nanofibers.

Fig. 5a. Nyquist plots of the EIS data of the as-made thin films on FTO glass with TZB-Gr nanofibers with different graphene centrifuged time durations. 5b. IMVS data measured under open-circuit conditions for films cast from TZB-Gr nanofibers with different graphene centrifuged time durations and TZB nanofibers. 5c. IMPS data for films cast from TZB-Gr nanofibers with different graphene centrifuged time durations and TZB nanofibers.

Fig. 6 – Comparing the DSC and TGA curves for TZB and TZB-Gr.

Scheme 1

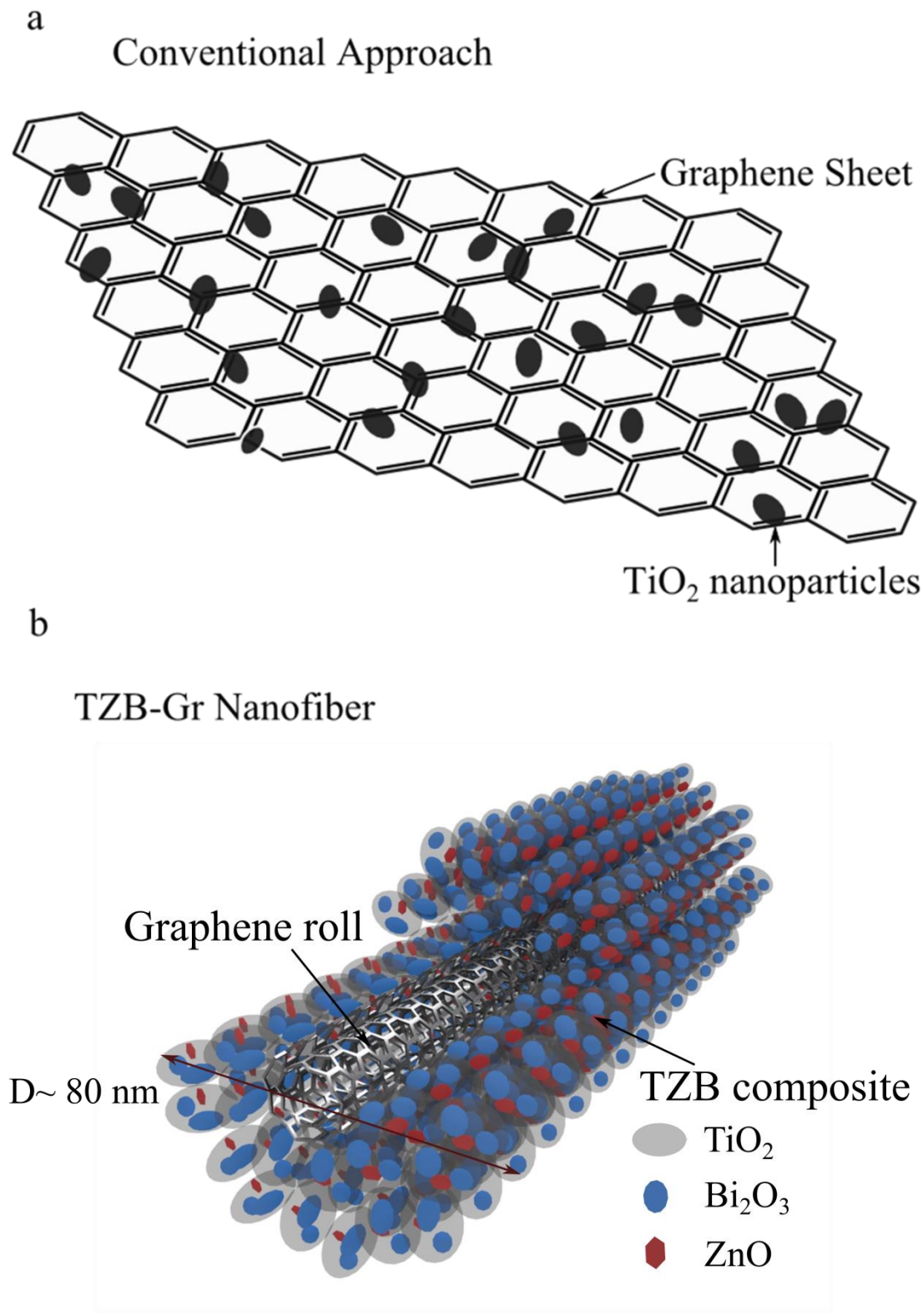
a
Conventional Approach
Graphene Sheet
$TiO_2$ nanoparticles
b
TZB-Gr Nanofiber
Graphene roll
D~ 80 nm
TZB composite
$TiO_2$
$Bi_2O_3$
ZnO

Fig.1

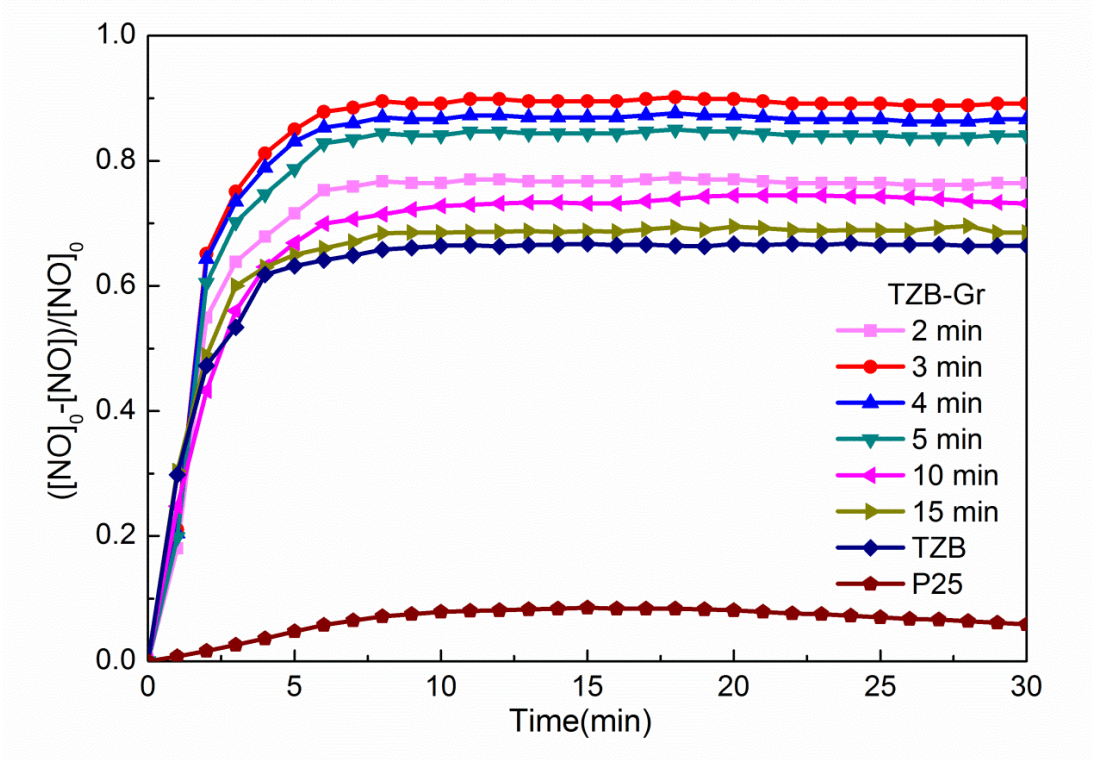
1.0
0.8
0.6
0.4
0.2
0.0
0
5
10
15
20
25
30
Time(min)
([NO]0-[NO])/[NO]0
TZB-Gr
2 min
3 min
4 min
5 min
10 min
15 min
TZB
P25

Fig. 2

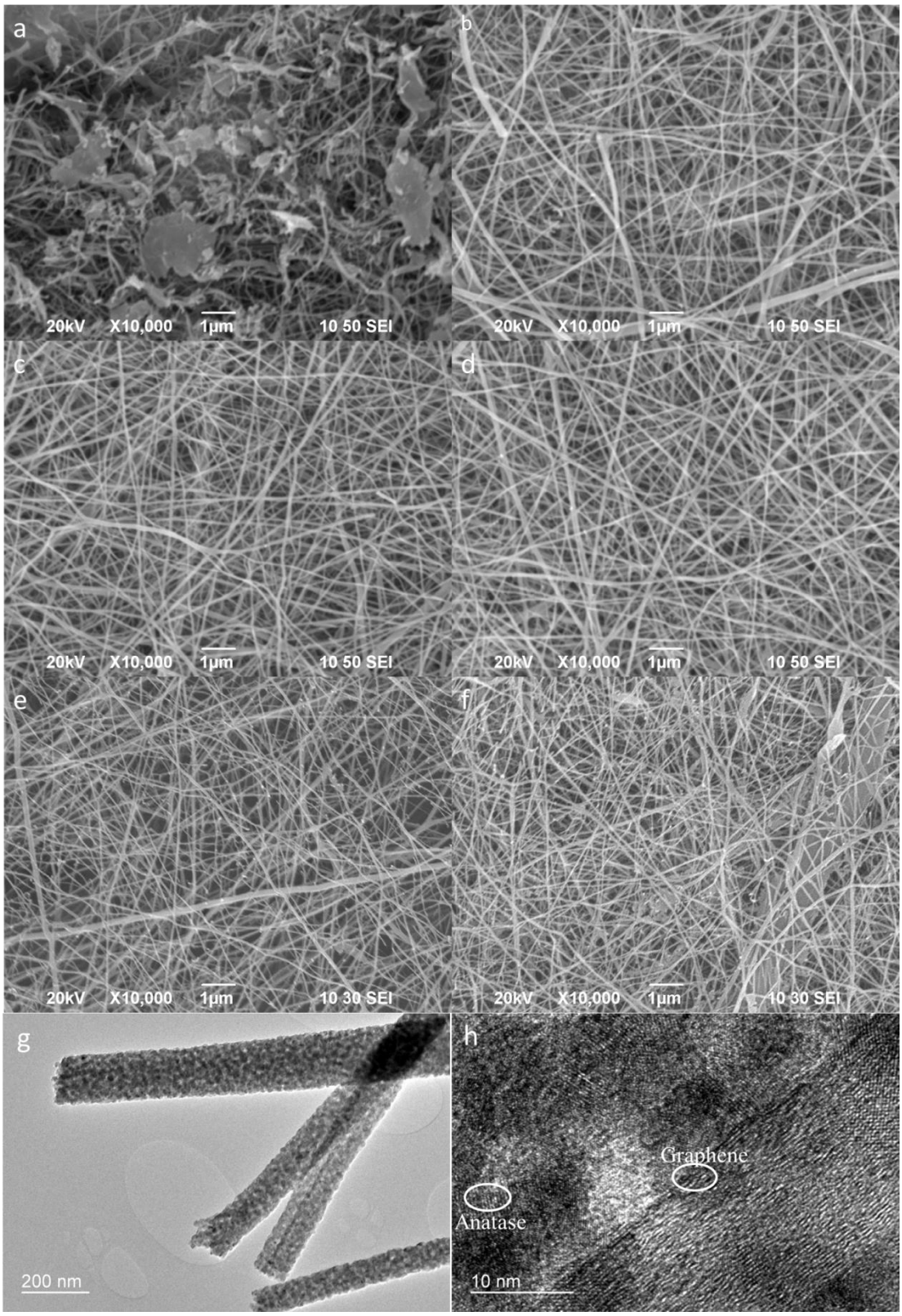
a
20kV X10,000 1μm 10 50 SEI
b
20kV X10,000 1μm 10 50 SEI
c
20kV X10,000 1μm 10 50 SEI
d
20kV X10,000 1μm 10 50 SEI
e
20kV X10,000 1μm 10 30 SEI
f
20kV X10,000 1μm 10 30 SEI
g
200 nm
h
Graphene
Anatase
10 nm

Fig. 3

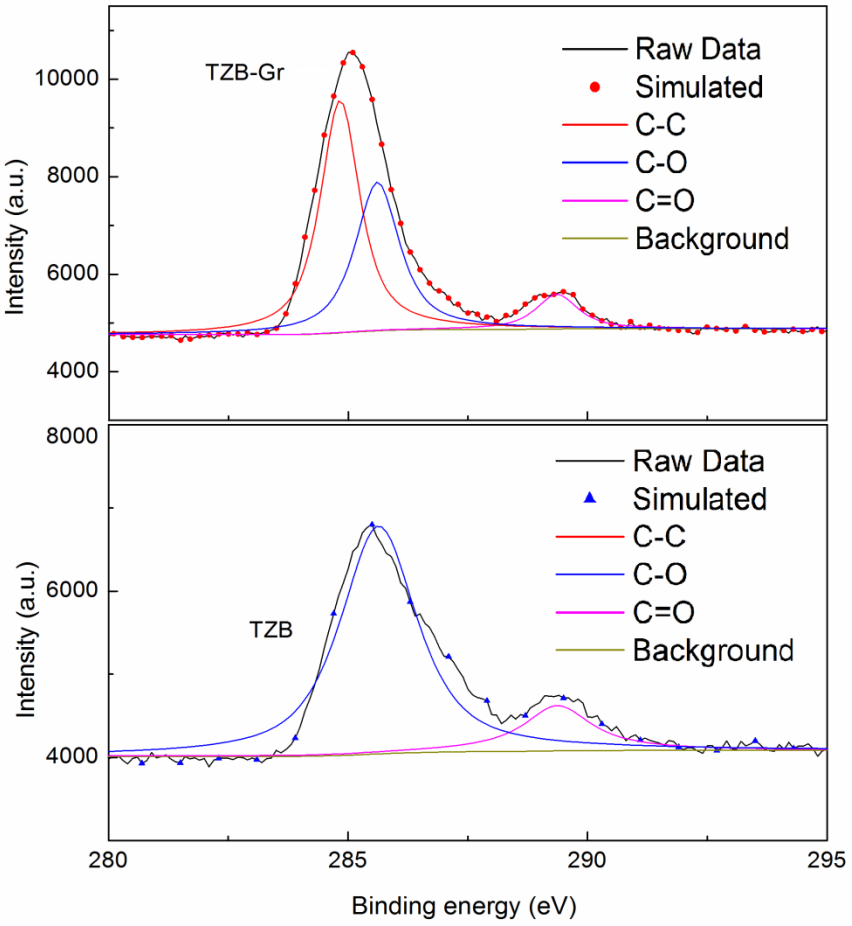
TZB-Gr
Raw Data
Simulated
C-C
C-O
C=O
Background
Intensity (a.u.)
10000
8000
6000
4000
TZB
Raw Data
Simulated
C-C
C-O
C=O
Background
Intensity (a.u.)
8000
6000
4000
280
285
290
295
Binding energy (eV)

Fig. 4

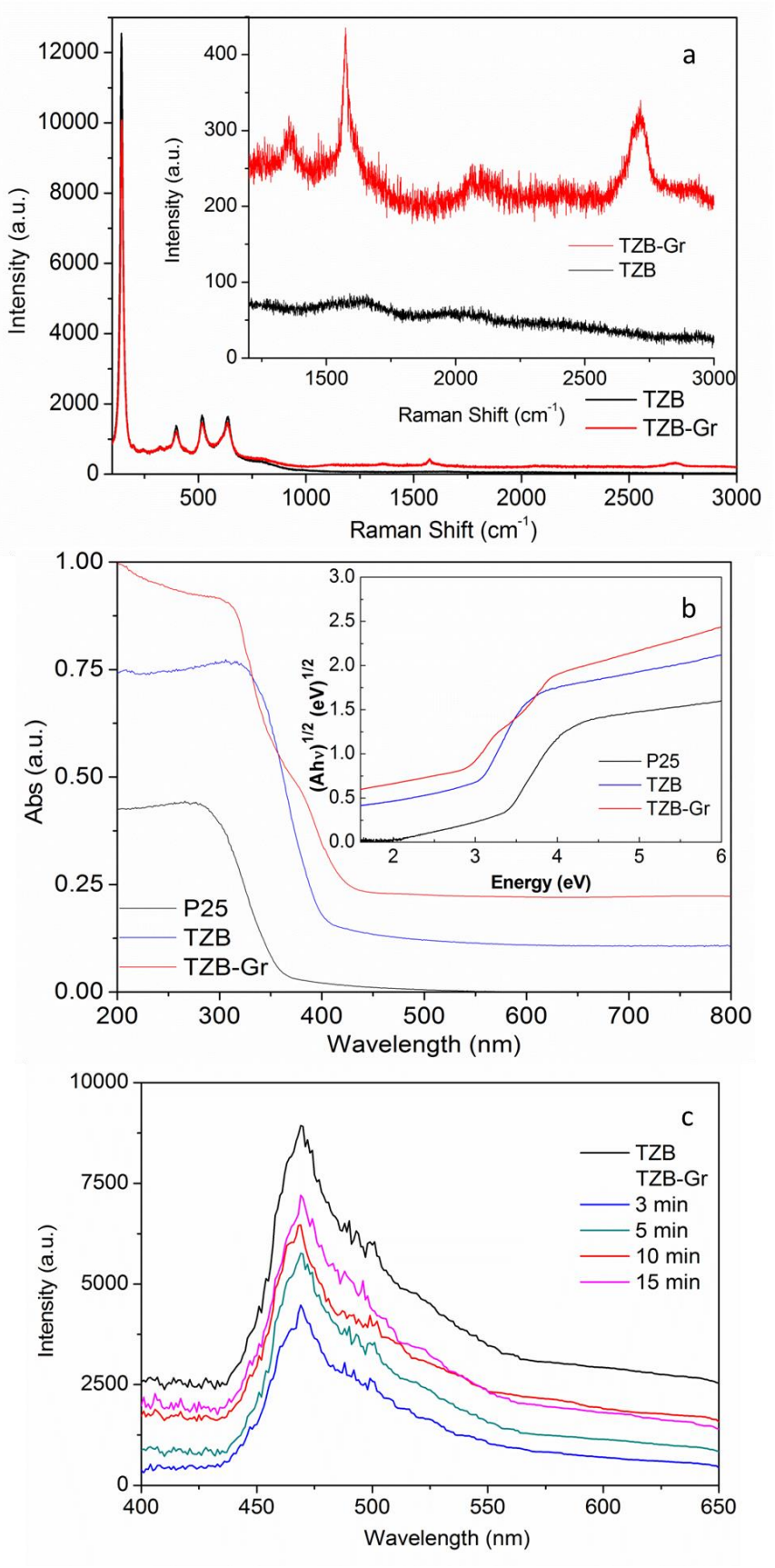
a
Intensity (a.u.)
Raman Shift (cm-1)
TZB-Gr
TZB
b
Abs (a.u.)
Wavelength (nm)
(Ahν)1/2 (eV)1/2
Energy (eV)
P25
TZB
TZB-Gr
c
Intensity (a.u.)
Wavelength (nm)
TZB
TZB-Gr
3 min
5 min
10 min
15 min

Fig. 5

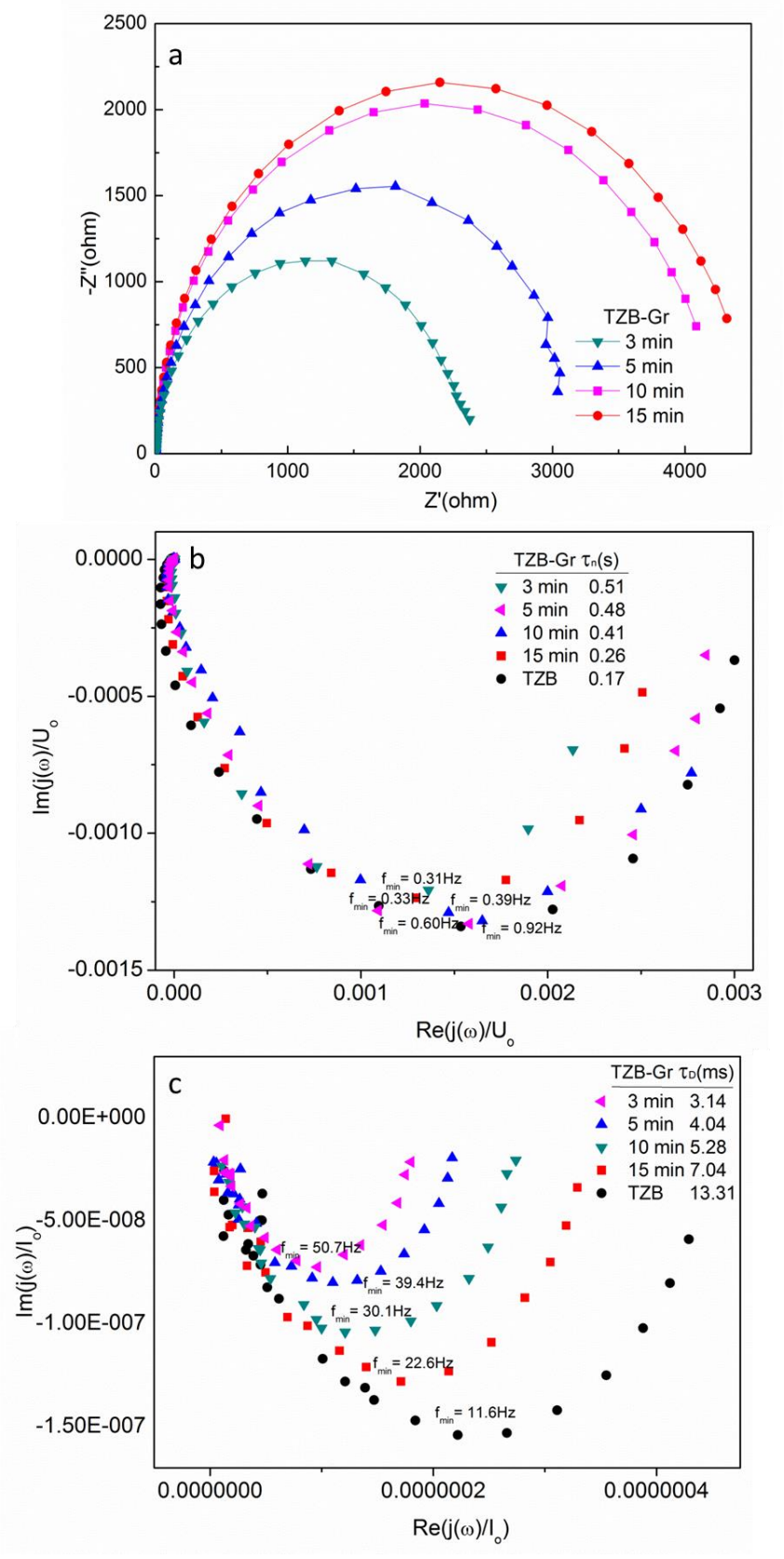
a
-Z''(ohm)
Z'(ohm)
TZB-Gr
3 min
5 min
10 min
15 min
b
Im(j(ω)/U_o
Re(j(ω)/U_o
TZB-Gr τ_n(s)
3 min 0.51
5 min 0.48
10 min 0.41
15 min 0.26
TZB 0.17
f_min = 0.31Hz
f_min = 0.33Hz
f_min = 0.39Hz
f_min = 0.60Hz
f_min = 0.92Hz
c
Im(j(ω)/I_o)
Re(j(ω)/I_o)
TZB-Gr τ_D(ms)
3 min 3.14
5 min 4.04
10 min 5.28
15 min 7.04
TZB 13.31
f_min = 50.7Hz
f_min = 39.4Hz
f_min = 30.1Hz
f_min = 22.6Hz
f_min = 11.6Hz

Fig. 6

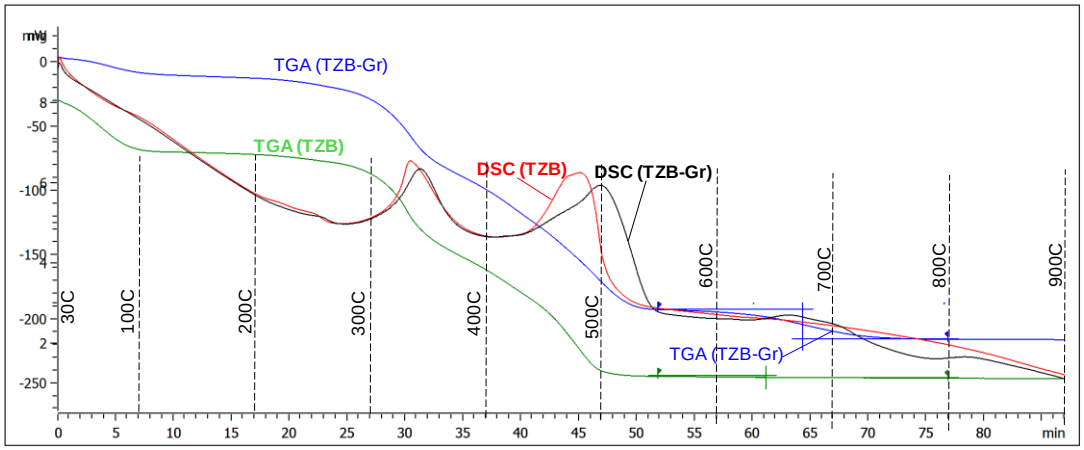
mW
0
8
-50
-100
-150
-200
-250
TGA (TZB-Gr)
TGA (TZB)
DSC (TZB)
DSC (TZB-Gr)
30C
100C
200C
300C
400C
500C
600C
700C
800C
900C
TGA (TZB-Gr)
0
5
10
15
20
25
30
35
40
45
50
55
60
65
70
75
80
min